Degradation Rates of the AVHRR Visible Channel for the NOAA 6, 7, and 9 Spacecraft

W. FRANK STAYLOR

Atmospheric Sciences Division, NASA Langley Research Center, Hampton, Virginia

(Manuscript received 4 May 1989, in final form 15 October 1989)

ABSTRACT

AVHRR channel 1 (0.57–0.69 μm) degradations were determined by comparing desert models with 68 months of observations of the Libyan Desert (20° to 30°N, 20° to 30°E). The comparisons revealed that the degradation rates were 0, 3.5% and 6.0% per year for NOAA 6, 7, and 9, respectively. An analysis based on zonal measurements covering half of Earth's surface suggests that these rates are applicable to all surface types.

1. Introduction

Radiance data from scanners on board NOAA's TIROS series of polar-orbiting satellites have been used to estimate local Heat Budget Parameters (HBP) on a global basis almost continuously since 1974 (Gruber and Winston 1978). Albedos are computed once per day from visible channel measurements taken during the daytime pass, while longwave fluxes are computed twice per day from infrared channel radiances taken during both the day and night passages. More recently, ISCCP (International Satellite Cloud Climatology Project, Schiffer and Rossow 1983) has undertaken an ambitious task to provide a 3-hourly, regional dataset that not only includes cloud parameters, but also many other meteorological parameters useful for global radiation budget studies (Schiffer and Rossow 1985; Darnell et al. 1988; Gupta 1989). Input data for ISCCP come from several geostationary satellites widely spaced along the Equator and from NOAA's TIROS-N series satellites. For ISCCP, the geostationary satellites provide coverage from the Equator to about 60° latitude, while the polar-orbiting satellite provides coverage for the polar regions. Differences in calibrations and spectral bandwidths of the geostationary satellite sensors are accounted for by normalizing their radiance measurements to those obtained by the TIROS satellite which underflies each of them every day. Thus, the accuracies of both the HBP and ISCCP datasets are directly tied to the long-term stability of the TIROS scanners.

The need for in-flight calibration became apparent in the early 1960s when radiometers exposed to the harsh space environment often degraded at alarming rates. Consequently, on board calibration systems were added to some instruments that generally took the form of solar diffuser plates, incandescent lamps, or both, for shortwave sensors and temperature-controlled blackbodies for longwave sensors (Williamson 1977). For instance, each of the three Earth Radiation Budget Experiment (ERBE) scanners launched during the 1984–86 time period had such in-flight calibration systems (Barkstrom 1984). The Advanced Very High Resolution Radiometer (AVHRR) scanners on NOAA's TIROS-N series satellites (1978 to present) have temperature-monitored blackbodies for the infrared channels, but unfortunately, no on board systems were included to assess the long-term stability of the visible channels in flight. Prelaunch ground calibrations of visible channel electronic gains have been used throughout the sensors' useful lifetimes in spite of the fact that some were operational more than 3 years (NOAA 7 and 9).

On board calibration systems can fail, degrade, or become unusable for numerous reasons, and their applicability is often questionable as they are usually activated in special calibration sequences that are substantially different from their operational Earth-viewing modes. Consequently, Staylor (1986) selected several desert sites which are used as natural Earth targets to provide an additional check on the stability of the ERBE scanners. In effect, the deserts become the solar diffuser plates and thermal blackbodies which will serve as long-term stable targets for comparisons. This approach allows comparisons among the three ERBE missions as well as comparisons between ERBE results and those of past and future radiation budget missions.

In the present paper, the Libyan Desert was used as a target site to assess the stability of the AVHRR scanners on board the NOAA 6, 7, and 9 satellites. A directional reflectance model permitted the degradation rates for the scanners to be determined from 68 months of observations beginning May 1980 and ending October 1987. Only channel 1 (0.57–0.69 μm) of the two

Corresponding author address: W. Frank Staylor, NASA/Langley Research Center, Mail Stop 420, Hampton, VA 23665-5225.

TABLE 1. Operation parameters for TIROS N series satellites.

Satellite	EXT[a]	GRC[a]	Launch date	Begin HBP	End HBP	Months[c]
TIROS N	0300–1500	9.3	13-10-78	1-1-79	20-1-80	0
NOAA 6	0730–1930	4.6	27-6-79	2-5-80	17-8-81	16
NOAA 7	0230–1430	8.6	23-6-81	22-8-81	30-1-85	31
NOAA 8	0730–1930	4.4	28-3-83	—	—	0
NOAA 9	0220–1420	9.5	12-12-84	2-2-85	31-10-87[b]	21
NOAA 10	0740–1940	4.6	17-9-86	—	—	0
NOAA 11	NA	NA	24-9-88	—	—	0
						68

[a] EXT and GRC at time of launch.
[b] Last data used in paper.
[c] Months used in paper.

AVHRR shortwave channels was studied as it is the only channel currently used in the HBP and ISCCP datasets. The present technique is relatively straightforward, particularly for Sun-synchronous satellites, and could be applied to a number of spacecraft with Earth-viewing scanners subject to shortwave degradation.

2. Satellites and measurements

a. *Satellites*

NOAA's first polar-orbiting, three-axis-stabilized meteorological satellites were the TIROS-M series. The first satellite (NASA-developed, prototype) of the M series was called ITOS-1, while the following five operational spacecraft were designated NOAA 1 through 5. All six were launched in the 1970–76 time period. The first satellite (NASA-developed, prototype) of the following N series was called TIROS-N, and the six operational spacecraft launched to date were designated NOAA 6 through 11. These seven spacecraft were orbited in the 1978–88 time period, and several more N series launches are planned. The initial HBP data (1974–78) were produced from Scanning Radiometers (SR) which were onboard the TIROS-M series spacecraft. However, the present paper is concerned only with the stability of the AVHRR scanners which were on board the TIROS-N series spacecraft, hence discussions will be limited to the N series.

The TIROS-N series satellites have been launched into Sun-synchronous orbits to nominal altitudes of 850 km and inclinations of 99°. TIROS-N and the odd-numbered spacecraft had equatorial crossing times, EXT, at about 0230 (descending) and 1430 (ascending) hours and are referred to as afternoon satellites because of their afternoon daylight orbital passes, while the even-numbered spacecraft had EXT at about 0730 (descending) and 1930 (ascending) hours and are referred to as morning satellites. Groundtrack repeat cycles, GRC, for the afternoon satellites were about 9 days, and about half that for the morning satellites. Values of EXT and GRC at launch are given in Table 1, and their relationship to the present analysis will be discussed and illustrated later.

b. *AVHRR*

The Advanced Very High Resolution Radiometer (AVHRR) is a crosstrack scanner that scans 110° (55° from nadir) six times per second. It has an instantaneous field of view of 1.3 milliradians for all channels which converts to a nadir resolution of about 1.1 km. The AVHRR has been flown in three configurations of channel number/bandwidth which are given in Table 2. Channels number 2, 3, and 4 had essentially the same half-power bandwidths for all seven satellites; however, channel 1 on TIROS-N was substantially broader than the others, and NOAA 7, 9, and 11 had an additional thermal channel (split window). The thermal channels view space and a temperature-monitored blackbody during each scan which permits their response stabilities to be determined in flight. No onboard systems were included to assess the response stabilities of shortwave channels 1 or 2. A more complete description of the AVHRR instrumentation and its operation is given by Schwalb (1978).

TABLE 2. Half-power bandwidths (μm) of AVHRR channels.

	Channel number				
Satellite	1	2	3	4	5
TIROS N	0.55–0.90	0.71–1.02	3.58–3.96	10.5–11.5	None
NOAA 6, 8, 10	0.57–0.69	0.72–0.99	3.56–3.94	10.5–11.5	None
NOAA 7, 9, 11	0.57–0.69	0.72–0.99	3.54–3.94	10.3–11.3	11.4–12.4

c. HBP dataset

Each channel of the AVHRR produces almost a billion measurements per day. While this massive quantity of high-resolution, multichannel data finds great utility in meteorological forecasting, it generally overwhelms climatologists whose requirements can often be satisfied with fewer spectral channels and less spatial resolution. This fact was recognized early during the TIROS program, and consequently, a number of satellite data products have been produced and archived by NOAA-NESDIS that are more compatible with user needs.

One such data product is the Heat Budget Parameters (HBP) dataset (Gruber 1977) where 484 pixels of AVHRR data from a 40 × 40 km subregion (nadir) are averaged for both channels 1 (0.57–0.69 μm) and 4 (10.5–11.5 μm). These averaged values were produced for 31 250 global subregions (125 × 125 for each hemisphere) that are located in a polar-stereographic grid.

The averaged channel 1 radiances, L_{sw}, are used to compute bidirectional reflectance as

$$R = \frac{\pi L_{sw}}{SU_0} \qquad (1)$$

where S is the Earth–Sun, distance-corrected, solar spectral flux for channel 1, and U_0 is the cosine of the solar zenith angle, θ_0; R is often equated to albedo, A, with the assumption of isotropy. The averaged channel 4 radiances are converted to broadband radiances (5–50 μm) with narrowband/broadband correlations (Gruber and Krueger 1984) that, in turn, are converted to longwave emission fluxes, E, with the aid of a limb-darkening model which is a function of viewing zenith angle, θ.

For each of the 31 250 subregions, albedos are computed once per day during the daytime orbital pass while longwave fluxes are computed for both the day and night passages. This 4 orders-of-magnitude reduction of AVHRR data volume allows 3 months of HBP data to be recorded on a single magnetic tape.

d. HBP data period

Periods for which HBP data are available from the TIROS-N series satellites are given in Table 1 and illustrated in Fig. 1. In general, only measurements from the afternoon spacecraft are used to produce HBP data because they offer better solar illumination conditions than do the morning spacecraft. However, with the sudden loss of TIROS-N data in January 1980, NOAA-NESDIS resorted to the NOAA 6 morning satellite until measurements from the NOAA 7 afternoon satellite became available in late August 1981. HBP data were produced continuously from NOAA 7 through January 1985. Measurements from the NOAA 9 afternoon spacecraft became available in February 1985 and continued until October 1988. Consequently, HBP data were not produced for the NOAA 8 morning satellite nor for the NOAA 10 (to date) morning satellite. However, in the future, NOAA-NESDIS plans to use AVHRR measurements from both the morning and afternoon satellites for HBP purposes and to base the albedo estimates on a composite of channel 1 and 2 radiances.

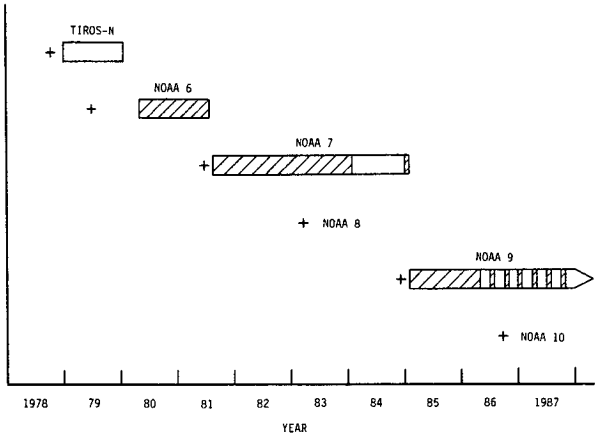

FIG. 1. Heat budget data available from the TIROS-N series satellite. Launch date denoted by +. Hatched areas indicate data used in present paper.

Normalized spectral responses of AVHRR channel 1 are presented in Fig. 2 for TIROS-N and NOAA 6, 7, and 9. Spectral responses for NOAA 6, 7, and 9 are quite similar; however, the bandwidth for TIROS-N was about 3 times that of the others. The near-infrared (0.7–0.9 μm) portion of the TIROS-N response, which for the others is essentially zero, is in a spectral region: 1) that overlaps water vapor absorption bands, and 2) where the reflectances of many surfaces (desert sand, vegetation, etc.) are greater than at visible wavelengths. For these and other reasons, the TIROS-N HBP data were not analyzed in the present paper because they are not compatible with results from NOAA 6, 7, and 9 nor future polar-orbiting NOAA satellites.

The author utilized HBP data tapes that were available from two ongoing studies at the NASA Langley Research Center. A GCM study provided tapes through February 1984, and the ERBE project provided tapes from January 1985 to April 1986 and every third month thereafter to October 1987 (see hatched areas, Fig. 1). As a result, HBP data from the NOAA 6, 7, and 9 satellites for 68 nonconsecutive months beginning in May 1980 and ending October 1987 are analyzed in the present paper.

3. Site selection

The present search for a desirable target site relied heavily on previous work performed by Staylor (1986) that was concerned with the selection and modeling of

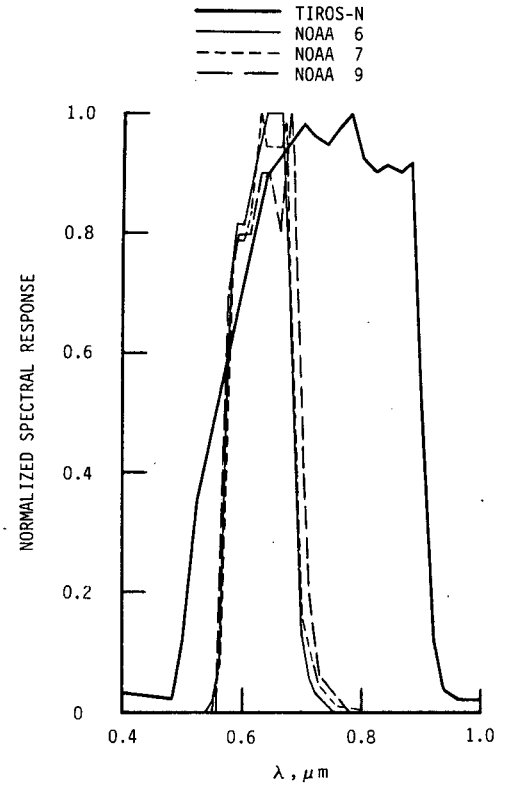

FIG. 2. Normalized spectral responses of AVHRR channel No. 1 for the TIROS-N series satellites.

sites to be used as ERBE validation targets. In that study, Staylor found that certain low-latitude deserts best met requirements of: 1) long-term stability, 2) high albedos combined with low solar zenith angles, 3) uniformity, 4) low cloudiness and low precipitation statistics, and 5) sufficient size. The primary site selected for ERBE scanner validations was the Saudi Desert (20.0°–22.5°N, 50.0°–52.5°E), and the Gibson Desert (25.0°–27.5°S, 120.0°–122.5°E) was selected as a secondary site for its better solar illumination conditions during October through March (primarily for the NOAA 10 morning satellite). However, only three HBP subregions lie within the boundaries of these 2.5° × 2.5° desert sites which were found to be insufficient for editing purposes, as discussed in the next section. Therefore, a much larger desert site with many more HBP subregions was necessary for the present study.

Nimbus-6 ERB scanner data and NOAA-7 AVHRR scanner data were used in the search for a desert with desirable properties and with sufficient size. The site chosen is located in northeastern Africa in part of a vast area generally known as the Sahara Desert. As seen in Fig. 3, this 10° × 10° area (20°–30°N, 20°–30°E) contains 54 HBP subregions and is centered about the Libyan/Egyptian border. Hereafter, the site will be referred to as the Libyan Desert since a large desert of that name covers the central portion of the area. The Libyan Desert site lies to the west of the Nile River and its tributaries and to the east of the Tibesti Mountains, both of which have undesirable, seasonal reflectance properties. It can generally be characterized as having vast expanses of sand dunes, sand seas, arid gravel, and rock outcroppings with very little moisture or vegetation (Short et al. 1976). On an annual basis, this site has one of the highest cloud-free, radiant fluxes of any comparable-sized area on Earth.

4. Data editing

HBP data for the Libyan Desert site were edited daily for missing data and for clouds. The editing was done in four sequential steps, denoted ES-1 through ES-4, meaning days eliminated in an earlier step were not considered for later steps. ES-1 was concerned with missing data, while ES-2, 3, and 4 were primarily concerned with clouds.

Editing for missing subregions is necessary here for two reasons. First, the Libyan Desert is not totally uniform, and therefore, if a substantial number of subregions were missing, the daily average of the remaining data could be biased. Second, when the spacecraft groundtrack passed to one side of the site, the majority of the missing subregions often tended to be grouped along the opposite side, meaning subregions viewed at the higher zenith angles were more frequently missing. The R is a function of θ, and therefore, this situation could also produce a biased result. Thus, an entire daily HBP dataset was eliminated if more than 4 of the possible 54 subregions were missing for that day. This editing procedure will be referred to as ES-1.

An inherent assumption for the present work is that the Libyan Desert site will provide a predictable reflectance target for an extended period of time. Gen-

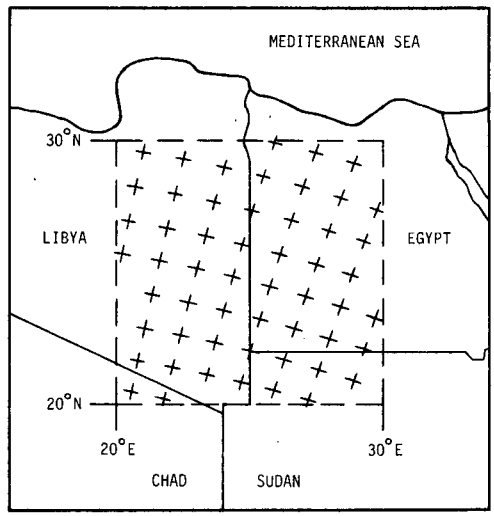

FIG. 3. Location of the Libyan Desert site, 20°–30°N, 20°–30°E (dashed lines). Locations of 54 HPB regions denoted by +.

erally, clouds increase reflectance, while sand storms and wet sand decrease reflectance, and the longwave emission fluxes are reduced for all three conditions. These conditions would violate the assumption of target predictability, and an attempt is made here to eliminate HBP datasets for as many days as possible for which these conditions exist.

Clouds, sand storms, and wet sand rarely cover the entire Libyan Desert, and when they do, it is usually not in a uniform manner. Therefore, daily dispersions of the longwave emission fluxes, σE, and the reflectances, σR, should provide a relative means for determining when these conditions may be present. Dispersion is defined here as the standard deviation of the 50 to 54 daily subregion measurements divided by the mean value of the measurements. Data from the NOAA 6 morning satellite will be used here to illustrate the cloud editing procedures as it had more severe solar illumination conditions than those for the NOAA 7 and 9 afternoon satellites.

In the bottom plot of Fig. 4, the daily values of σE (397 of 473 that survived ES-1) are presented for the entire NOAA 6 dataset (2 May 1980 to 17 August 1981). Analyses indicated that for $\sigma E > 0.05$ the reflectances were often greater than their expected values. Therefore, $\sigma E = 0.05$ (dashed line) was used as a threshold editing value for NOAA 6, 7, and 9, and will be referred to as ES-2.

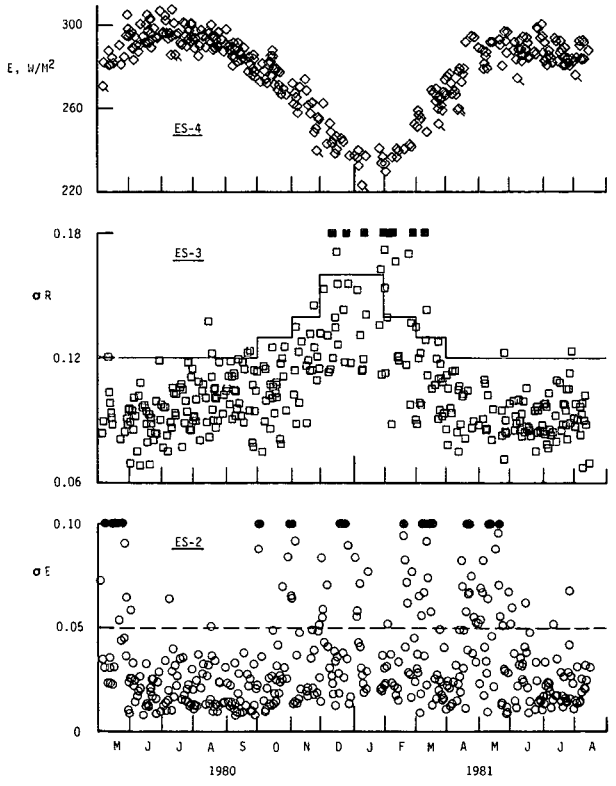

FIG. 4. Illustration of cloud editing procedures for NOAA 6 data. $\sigma E > 0.10$ plotted solid at 0.10. $\sigma R > 0.18$ plotted solid at 0.18.

TABLE 3. Data editing summary.

	NOAA 6	NOAA 7	NOAA 9	SUM
Total days[a]	473	943	638	2054
Pass ES-1	397	869	527	1793
Pass ES-2	314	588	380	1282
Pass ES-3	289	533	349	1171
Pass ES-4	279	514	337	1130

[a] For periods used in paper.

Daily values of σR (314 of 397 that survived ES-2) are given in the middle plot of Fig. 4. The general level of σR increased with solar zenith angle, which, for NOAA 6, ranged from 55° during the summer months to 77° during the winter. The R is also a function of $\cos\theta_0$, and therefore, the ±5° range of θ_0 across the 10° × 10° Libyan Desert site became an important source of dispersions for NOAA 6 during the fall to spring months. As a result, the σR threshold values for NOAA 6 were varied from 0.12 for April through September, 0.13 for October and March, 0.14 for November and February, to 0.16 for December and January (solid lines). The solar zenith angles for NOAA 7 and 9 during the winter months never exceeded those of NOAA 6 for April and September, and therefore, their threshold values were set at $\sigma R = 0.12$ for all months. This editing step will be referred to as ES-3.

There was some concern that thin cirrus clouds or perhaps a sand storm might uniformly cover the site and go undetected by the dispersion methods of ES-2 or -3. Consequently, the relative values of longwave emission fluxes were used as a final editing parameter. In the top plot of Fig. 4, the daily values of E (289 of 314 that survived ES-3) are given, and 10 values (flagged) that were 10 W m^{-2} or more below the main sequence of data were eliminated from the dataset. This editing procedure was performed visually and will be referred to as ES-4.

A data editing summary is given in Table 3 for NOAA 6, 7, and 9 for each editing step. Of the initial total of 2054 days, 1130 days (55%) survived all four editing procedures. The vast majority (98%) of the 1793 days that passed ES-1 had data from all 54 subregions present, while most (56%) of the 261 days eliminated had none at all. ES-2 eliminated the most days (25%); however, this was due mainly to its position in the editing sequence. Had ES-3 (σR) been placed ahead of ES-2 (σE), it would have eliminated the most days. Subsequent comparisons of R for the 41 days eliminated by ES-4 indicated that most were at expected levels, meaning that cirrus clouds or sand storms were probably not present on these days. However, none of these edited days were included in the dataset.

The present analysis is based on monthly results, and therefore, the number of days available each month

is important. June through November were the clearest months having an average of about 22 days available per month, while December through May were the cloudiest months with an average of only 12 days. All 31 days for August 1982 (NOAA 7) passed the editing requirements, but only 8 days passed for March 1985 (NOAA 9) primarily because 12 days failed ES-1. Missing days (ES-1) generally occurred at random times throughout the dataset; however, March 1985 had 7 consecutive days missing. The end of the NOAA 6 dataset occurred during August 1981 (see Table 1) and was counted as 1 of its 16 data months since 13 of 17 available days met the editing requirements. The beginning of the NOAA 7 dataset also occurred during August 1981, but it was not counted as 1 of its 31 data months since only 6 of 10 available days passed editing.

5. Data cycles

The procedure for determining the radiometric stabilities of the AVHRR scanners on board the NOAA 6, 7, and 9 spacecraft might have been a relatively simple task. Stabilities could have been based on comparisons of monthly averaged site reflectance with those obtained for the same months in subsequent years when the solar illumination conditions were identical. Unfortunately, there are two problems with this procedure. One involves edited days combined with the cyclic behavior of the measured reflectances. The other problem is concerned with the fact that the NOAA spacecraft are not in truly Sun-synchronous orbits, and hence, their solar illumination conditions are not repeated each year.

The cyclic behavior of the daily measured bidirectional reflectance for the Libyan Desert site is illustrated in Fig. 5. These data were taken by NOAA 9 during a cloud-free period from 1 August to 20 September 1985 (August 7 and 27 edited by ES-1). If a number of random days were edited from the plot, the average value of R might not be greatly affected; however, it is not certain that this will always be the case as many of the winter and spring months have most of their days edited.

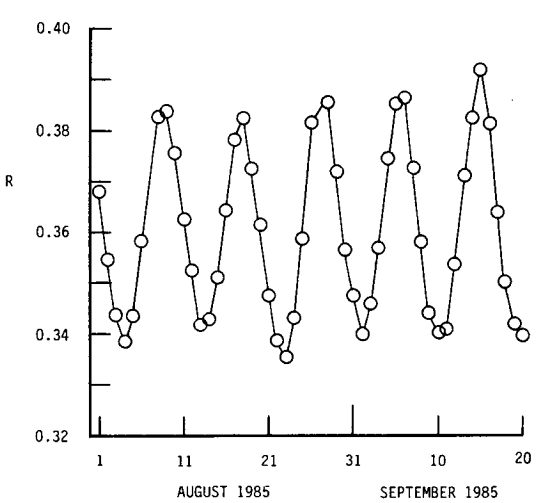

FIG. 5. Illustration of the cyclic behavior of the bidirectional reflectance for the Libyan Desert site measured by NOAA 9.

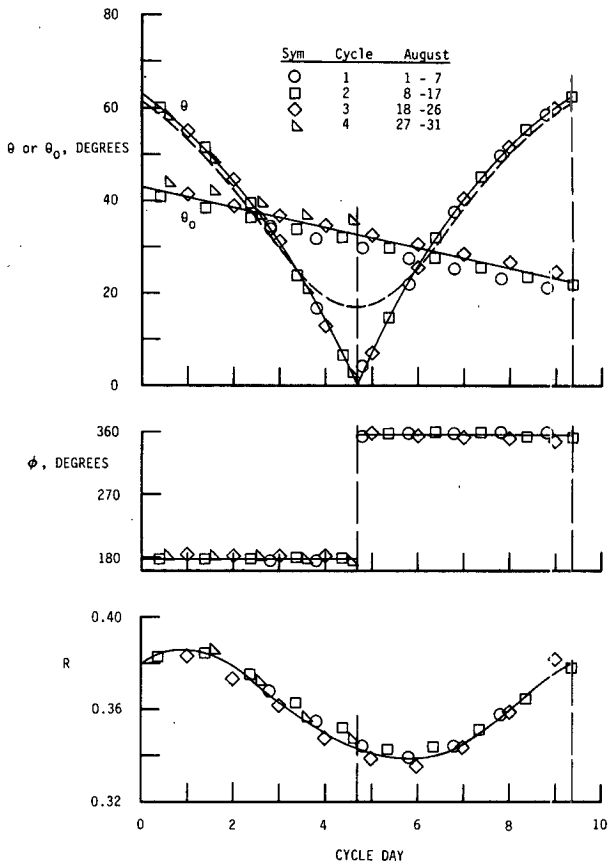

FIG. 6. Angular parameters for NOAA 9, August 1985.

The cyclic behavior of R is related to the cyclic pattern of the angular parameters involved which are illustrated in Fig. 6 for the August 1985 data (calculated for the site center, dashed curve average θ for entire site). Viewing zenith angle θ, solar zenith angle θ_0, azimuth angle ϕ, and R are plotted along a 9.4-day cycle determined by the groundtrack repeat cycle (GRC) of the satellite (GRC decreased a few percent per year for each of the satellites). For the afternoon spacecraft (GRC $\approx$ 9 days), this means that a fixed point on Earth is viewed for the first 3 days of the cycle at large angles from the east, then for 3 days at small angles near nadir, and lastly for 3 days at large angles from the west; then the cycle repeats. Solar zenith angle decreases linearly during the cycle, while azimuth angle is constant at $\phi \approx 180°$ (back-reflectance) for the first half of the cycle, then shifts abruptly 180° to $\phi \approx 360°$ (forward-reflectance) for the last half of the cycle. In general, R increases with both θ and θ_0 and is higher for back-reflectance (Staylor and Suttles 1986), but

the primary cause of its cyclic behavior seen here is due to the cyclic pattern of θ.

The solar zenith angle at a site during overpass of a truly Sun-synchronous satellite (i.e., constant equatorial crossing time, EXT) varies only with solar declination and analemma, both of which have yearly cycles. To within several minutes, NOAA 6 remained at its launch EXT throughout its operational lifetime. However, both NOAA 7 and 9 precessed to later EXT at rates ranging from 15 to 30 minutes per year. For instance, the NOAA 7 afternoon EXT was 1430 at launch in June 1981, but precessed to 1600 by January 1985. These precessions caused the solar zenith angles for NOAA 7 and 9 to cycle to higher values as illustrated at the bottom of Fig. 7 for the Libyan Desert and NOAA 9. While there are two periods each year for which midlevel values of θ_0 are matched (etc 45°), the azimuth angles are not simultaneously matched. Thus, all solar illumination conditions are never totally repeated for the quasi-Sun-synchronous NOAA 7 and 9 spacecraft. It is clear that a bidirectional reflectance model is needed to assess the scanner stabilities because of the nonisotropic properties of the Libyan Desert combined with the nonrepeating illumination conditions.

6. Reflectance and degradation models

The bidirectional reflectance model used by Staylor (1985) to characterize clouds and by Staylor and Suttles (1986) to characterize deserts is given by

$$Y = Y_0 + Y_1 X^N \qquad (2)$$

where $X = UU_0/(U + U_0)$, $Y = \bar{R}UU_0$, $U = \cos\theta$ and $U_0 = \cos\theta_0$. This model exhibits zenith angle reciprocity (i.e., θ and θ_0 interchangeable) and was found to be applicable over a wide range of zenith angles. A general discussion of the physical significance of the regression coefficients Y_0, Y_1, and N is given by Staylor (1985).

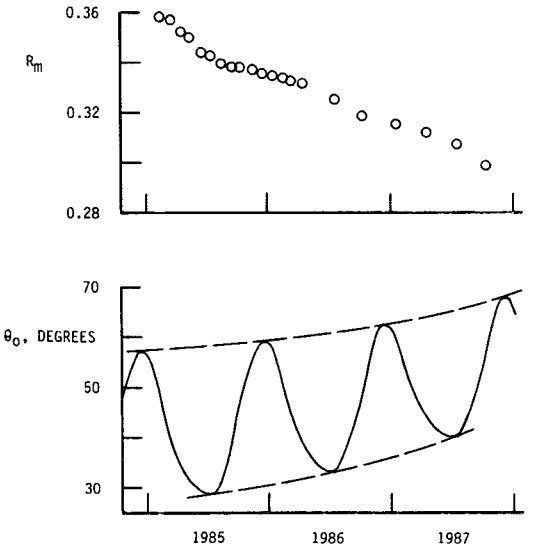

FIG. 7. Monthly minimum reflectances and corresponding solar zenith angles for NOAA 9.

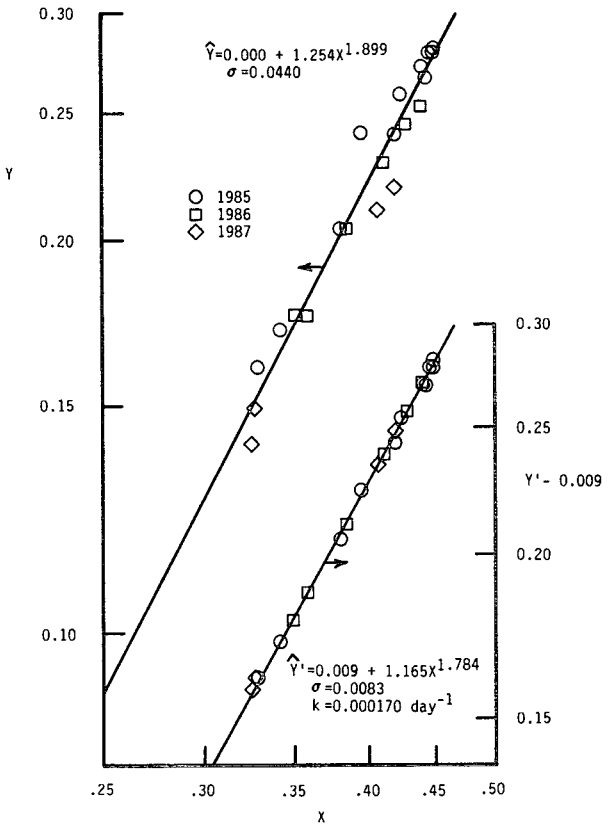

FIG. 8. Correlation of the X and Y parameters, NOAA 9. Left scale initial fit, right scale final fit.

For deserts, $\bar{R} = R/P$ where P is an azimuthal parameter which is a function of ϕ, θ, and θ_0 (Eq. (6), Staylor and Suttles 1986). However, if either of the zenith angles is at nadir (θ or $\theta_0 = 0°$), $P = 1$ and the azimuthal dependence of Eq. (2) is totally eliminated. The minimum reflectance, $R_m = 0.34$, in Fig. 6 does not occur at $\theta = 0°$ (day 4.7), but does occur at a sufficiently small angle such that $P \approx 1$, hence $\bar{R} \approx R_m$. This approximation eliminates ϕ and θ as variables and reduces the model to a function of only θ_0.

Cyclic plots of R such as shown at the bottom of Fig. 6 were prepared and R_m determined for all 68 months of data used in this paper. The minimum reflectances for NOAA 9 are given at the top of Fig. 7, and from the continuous decline of the values it is clear that substantial sensor degradation occurred during the 3-year period. A method for determining sensor degradations will be described in the following paragraphs and figures. The procedure involves several iteration steps of which only the first and last will be illustrated.

With $\bar{R}$ set equal to R_m and U set equal to 0.94, the 21 monthly values of Y and X for NOAA 9 are plotted on a log–log scale at the top of Fig. 8 (left scale). A

linear regression fit to the data gives $Y_1 = 1.254$ ($X = 1$ intercept) and $N = 1.899$ (slope). Because of the large data scatter, no attempt was made at this point to evaluate Y_0 which, in essence, was set equal to zero. In spite of the scatter, it can be seen that, in general, the 1985 data (circular symbols) lie above the line, the 1986 data (squares) lie near the line, and the 1987 data (diamonds) lie below the line.

The initial model, $\hat{Y} = 1.254(X)^{1.899}$, was then used to compute values of $Y/\hat{Y}$ which are presented at the top of Figure 9 as a function of the number of days after spacecraft launch, d. A degradation model of the form

$$D^{-1} = \exp(-kd) \tag{3}$$

was assumed as the stabilities of many electronic instruments often degrade exponentially with use or exposure. The initial value of the degradation rate, k, was determined to be 136×10^{-6} per day which was then used to correct Y as

$$Y' = DY. \tag{4}$$

Then Y' was plotted versus X as in Fig. 8 (right scale), and the data scatter was reduced significantly such that a value of Y_0 as well as new values of Y_1 and N could be determined. This new model was used to compute $Y/\hat{Y}'$, and a new value of k was determined. After several more similar iterations, a near-minimal dispersion, $\sigma Y'$, was obtained, and the results are shown at the bottoms of Figs. 8 and 9. The dispersion was reduced by a factor of 5 from the initial step and the data for all 3 years now lie on the line. The degradation rate was estimated to be 170×10^{-6} per day which converts to about 6% per year. From launch in mid-December 1984 to mid-October 1987 (last data month of paper), the response of the NOAA 9 AVHRR channel 1 sensor degraded 16% which will increase to about 21% by October 1988 (NOAA 11 replaced NOAA 9 in November 1988).

Data from the NOAA 7 spacecraft were processed in an iteration procedure similar to that used for NOAA 9. Initial and final plots of Y and $Y' - Y_0$ versus X for NOAA 7 are presented in Fig. 10, and the degradation rate was estimated to be 98×10^{-6} per day or about

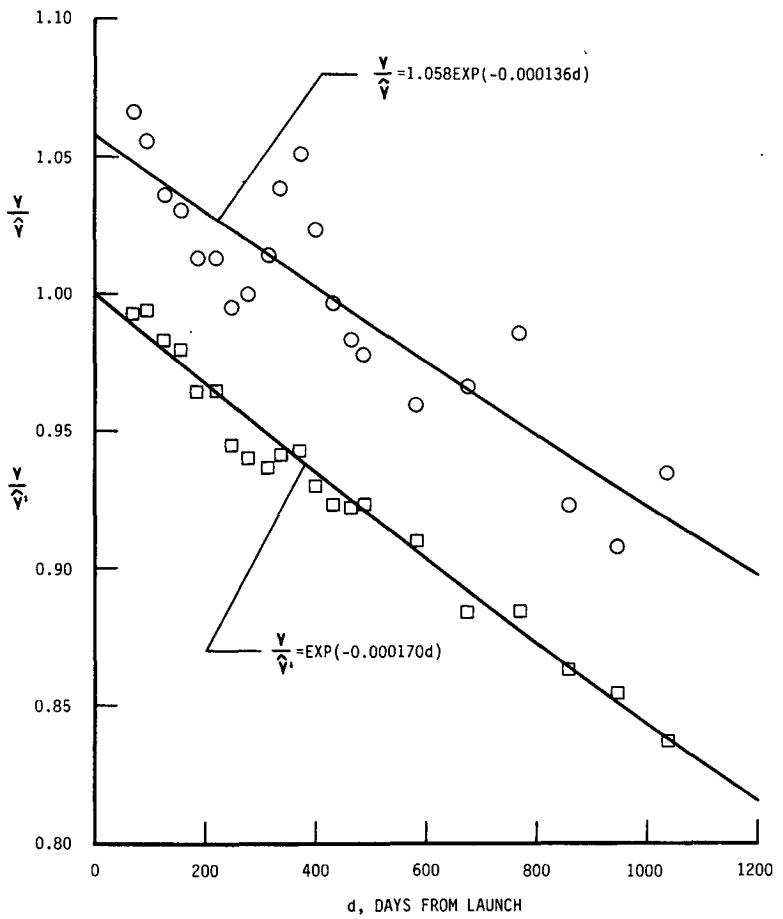

FIG. 9. Degradation trend of the NOAA 9 AVHRR channel 1.

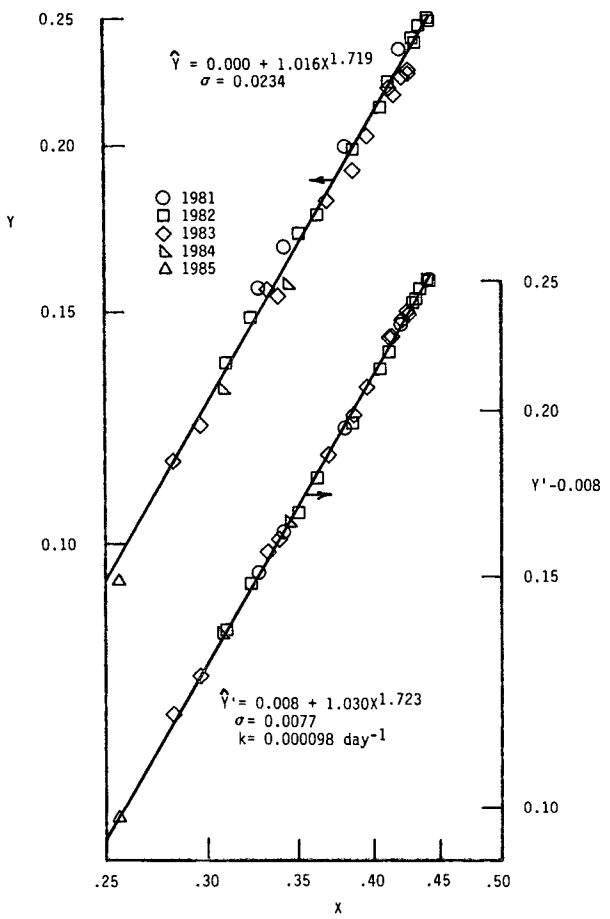

FIG. 10. As in Fig. 8 except for NOAA 7.

3.5% per year. The identical procedure was also used for NOAA 6, but as seen in Fig. 11, no degradation of its sensor was detectable during the 16 months from May 1980 to mid-August 1981 (i.e., $k = 0$, $D = 1$, $Y = Y'$). All model parameters for the NOAA 6, 7, and 9 spacecraft sensors are given in Table 4.

7. Discussion of results

The degradation-corrected models of $Y' - Y_0$ are shown at the top of Fig. 12 for the X ranges of the NOAA 6, 7, and 9 Libyan Desert data, and it can be seen that the corrected models do not estimate identical values of Y' (hence R' and L'). These differences may be due to differences in the spectral responses of the three scanners (see Fig. 2) or perhaps due to errors in the prelaunch, ground-calibrations of their electronic gains which were used throughout their operational lifetimes. But whatever the cause(s), radiance data from the three satellites must be normalized to a consensus value in order for the measurements to be properly utilized for HBP, ISCCP, or other long-term climatological purposes.

The NOAA 7 dataset was chosen here as the normalizer because: 1) its model was based on more months of data (see Table 1), 2) its X range overlapped the others better, and 3) its values were between those of NOAA 6 and 9. NOAA 6 and 9 data were each normalized by a factor, B_i, as

$$Y_i'' = B_i Y_i' \tag{5}$$

with B_7 set equal to unity for the NOAA 7 data. All 68 months of data from the three satellites were processed to produce a minimal σ, and the computed normalization factors for NOAA 6 and 9 were 1.052 and 0.935, respectively. The resulting Y'' values are presented at the bottom of Fig. 12, and the combined-model parameters are given in Table 4.

It is recommended that the following degradation and normalization corrections be made to radiance measurements from AVHRR channel 1 for the NOAA 6, 7, and 9 sensors.

NOAA 6: multiply times 1.052;
NOAA 7: multiply times 1.000 $\exp(98 \times 10^{-6} d_7)$, $d_7 = 0$ on 23 June 1981;
NOAA 9: multiply times 0.935 $\exp(170 \times 10^{-6} d_9)$, $d_9 = 0$ on 12 December 1984.

The accurate computation of the daily varying angles ϕ, θ, and θ_0, such as illustrated in Fig. 6, requires an accurate knowledge of the satellite's orbital ephemeris

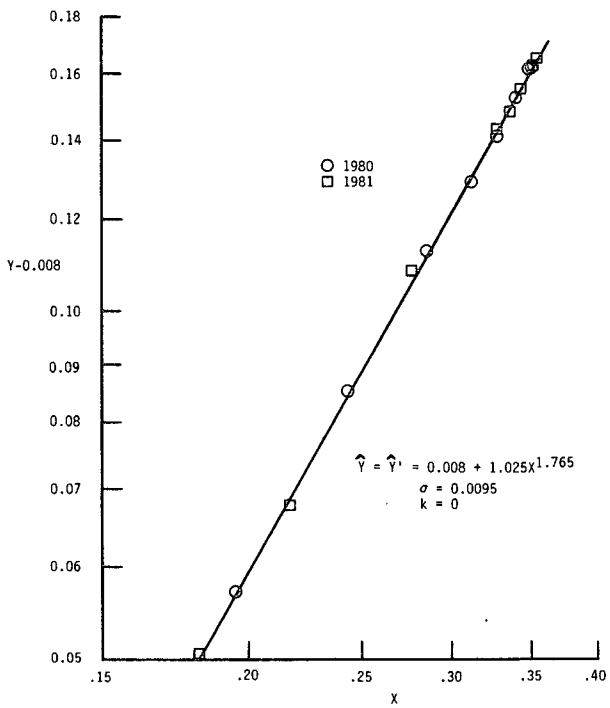

FIG. 11. Correlation of the X and Y parameters, NOAA 6.

TABLE 4. Model parameters for the Libyan Desert.

Satellite	Estimate	Y_0	Y_1	N	$k \times 10^6$	$\sigma Y'$	B
NOAA 6	$\hat{Y} = \hat{Y}'$	0.008	1.025	1.765	0	0.0095	1.052
NOAA 7	$\hat{Y}'$	0.008	1.030	1.723	98	0.0077	1.000
NOAA 9	$\hat{Y}'$	0.009	1.165	1.784	170	0.0083	0.935
Combined	$\hat{Y}''$	0.008	1.048	1.740	—	0.0093	—

and moderate computer resources. However, the minimum reflectance technique used in the present paper ($\bar{R} = R_m$) requires only the calculation of U_0 and the evaluation of R_m from time plots of R such as given in Fig. 5. The equation for U_0 is given by

$$U_0 = \sin(\mathrm{DEC})\sin(\mathrm{LAT}) + \cos(\mathrm{DEC})\cos(\mathrm{LAT}) \times \cos[(12 - \mathrm{EXT}) \times 15° - \alpha + \beta] \quad (6)$$

where DEC is the solar declination, LAT the latitude of the site center, α the analemma, and $\beta = \pm\arcsin[\tan(\mathrm{INC} - 90°)\tan\mathrm{LAT}]$ where INC is the orbital inclination and the plus sign (+) is used for ascending daylight orbits such as NOAA 7 and 9 (NOAA 6 descending). DEC and α vary with day-of-year and can be obtained from tables. As mentioned previously, the crossing time, EXT, for the NOAA-N series satellites changed throughout their operational lifetimes, but INC remained virtually constant (99°). Both EXT and INC are available from NOAA tracking facilities. Thus, the present technique can be applied to future NOAA satellite data with only minimal requirements of time and resources.

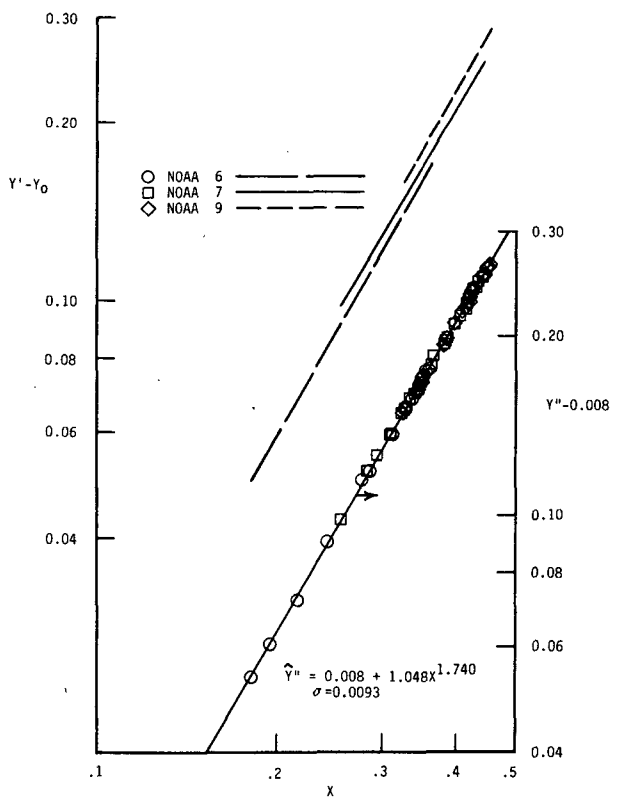

FIG. 12. Combination of data from NOAA 6, 7, and 9 into a single Libyan Desert model. Note stepped vertical scale.

Model parameters for the Sahara–Arabian and Saudi deserts determined from broadband Nimbus 7 scanner measurements (Staylor and Suttles 1986), and the NOAA 6, 7, and 9 combined parameters for the Libyan Desert are given in Table 5. The Libyan Desert (10° × 10°) and, in particular, the Saudi Desert (2.5° × 2.5°) are relatively small, but bright areas located within the vast area referred to as the Sahara–Arabian Desert (15° × 70°). Albedos for the three deserts were computed from the model parameters and are presented in Fig. 13 as a function of U_0. The Sahara–Arabian and Saudi desert albedos were based on solar zenith angle data for the U_0 = 1.0 to 0.6 range and were model-extrapolated to U_0 = 0.18 using viewing zenith angle reciprocity, while the Libyan desert albedos were based on solar zenith angle data for the U_0 = 0.88 to 0.18 range with model-extrapolation only to U_0 = 1.0. All three deserts have similar increasing-albedo trends in the U_0 = 1.0 to 0.6 range; however, the Libyan desert albedos approach an asymptotic level at about U_0 = 0.2 while the others continue to increase. This trend difference at large solar zenith angles is probably the result of the greater influence that unsaturated Chappuis ozone absorption (0.5–0.7 μm) has on narrowband (0.57–0.69 μm) relative to broadband (0.2–4 μm) measurements at large atmospheric path lengths (approximately proportional to U_0^{-1}).

A general classification of satellite-observed scene "colors" on a scale from blue to red would place clear oceans at the blue end of the spectrum followed by ice/snow, clouds, vegetation/forest, with deserts at the red end of the spectrum. The fact that deserts are "redder" than most other scene types led the author to question whether the sensor degradations reported here are applicable to them as it seemed quite possible that sensor degradations at shorter wavelengths might be different (greater or less) than those at longer wavelengths (see Fig. 2). Detailed analyses of several other scene types, such as the one performed here for the

TABLE 5. Model coefficients for bright deserts.

Desert	Satellite	λ, μm	Y_0	Y_1	N
Sahara–Arabian	Nimbus 7	0.2–4	0.011	0.920	1.764
Saudi	Nimbus 7	0.2–4	0.008	1.088	1.678
Libyan	NOAA-Combined	0.57–0.69	0.008	1.048	1.740

Libyan Desert, might provide the answer. Unfortunately, virtually no other scene type has a combination of long-term stability, high reflected radiances, and positive cloud identification that would be needed to detect small degradation differences among scene types. Therefore, reflection measurements from a large site that included most scene types were analyzed with the basic assumptions that: (1) the interannual monthly variations are small, and (2) if the degradations for the multiscene site were approximately those determined for the Libyan Desert, the spectral degradation is probably uniform across the response bandwidth, and hence, applicable to all scene types.

The "site" chosen for this analysis includes all latitudinal zones from 30° north to 30° south (i.e., half the Earth's surface) which offers the following advantages: 1) this 60° zonal area contains all scene types of interest except ice/snow; 2) because the area has little seasonal ice/snow or vegetation cover, it should have minimal interannual monthly variations; 3) its low latitudes (30° maximum, equator-centered) have relatively small satellite-observed, solar zenith angle variations; and 4), the site's size provides adequate sampling.

All NOAA 9 daily HBP reflectance measurements within the 60° zone were used in the analysis for the months April, July, and October 1985 and January, April, July, and October 1986. With the assumption of isotropy ($A = R$), approximately a half-million measurements per month were used to compute a monthly averaged zonal albedo as

$$\bar{A} = \frac{1}{2\pi}\int_0^{1\ \text{month}} \int_{-\pi/6}^{\pi/6} \int_0^{2\pi} A\, d(\text{LONG}) \times \cos(\text{LAT})\, d(\text{LAT})\, d(t) \quad (7)$$

where LONG is longitude and t is time. The seven computed monthly albedos shown at the top of Fig. 14 (circular symbols) appear to reach maximum values in October with minimum values occurring in June/

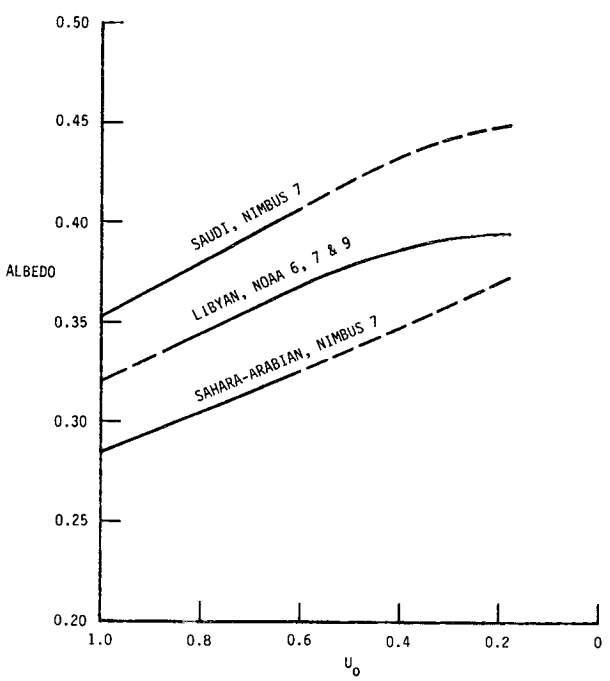

FIG. 13. Desert albedos derived from satellite scanner measurements. Solid lines are U_0 range of data, dashed lines are model extrapolations.

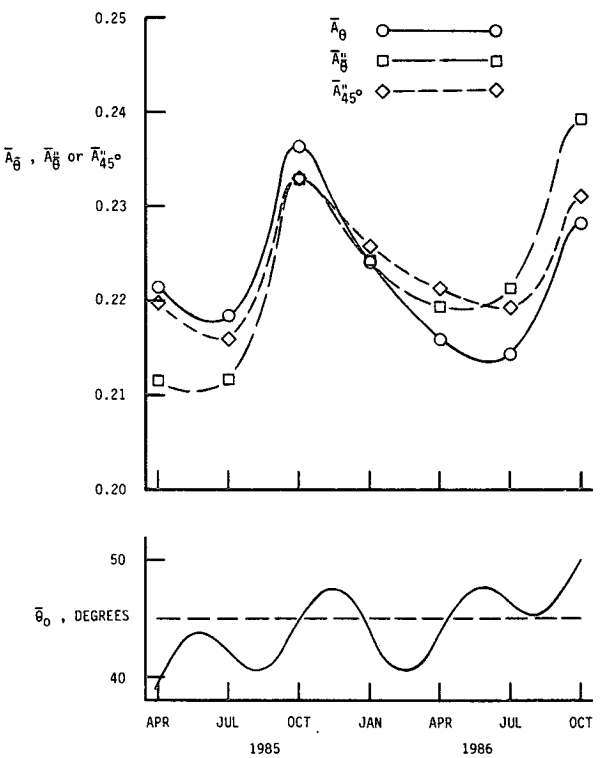

FIG. 14. Sixty-degree zonal albedos, NOAA 9.

TABLE 6. NOAA 9 60°-zonal albedo comparisons.

	$\overline{\text{AJO}}$ 1985	$\overline{\text{AJO}}$ 1986	Difference
$\bar{A}_{\bar{\theta}_0}$, uncorrected	0.2254	0.2195	−2.6%
$\bar{A}''_{\bar{\theta}_0}$, corrected for D	0.2187	0.2266	+3.6%
$\bar{A}''_{45°}$, corrected for D and $\bar{\theta}_0$	0.2229	0.2239	+0.4%

July. These albedos were corrected for sensor degradation and normalization as

$$\bar{A}'' = \bar{A}[0.935 \exp(170 \times 10^{-6}\bar{d}_9)] \qquad (8)$$

where $\bar{d}_9$ was the midmonth day. These values are also shown in Fig. 14 (square symbols).

Albedo values for April, July, and October were averaged ($\overline{\text{AJO}}$) for both 1985 and 1986 and are compared in Table 6. The uncorrected 1986 average albedo was 2.6% less than the 1985 average while the degradation-corrected 1986 average albedo was 3.6% larger than the 1985 value. This latter comparison might suggest that the present degradation corrections which were based on Libyan Desert measurements are too large, and hence, are not applicable to other "bluer" scene types. However, as mentioned previously, this comparison is not valid because the satellite-observed, solar illumination conditions for 1986 did not repeat those for 1985. This fact is illustrated at the bottom of Fig. 14 where the mean satellite-observed, solar zenith angles, $\bar{\theta}_0$, for the 60° zone are seen to cycle to higher angles as they did for the Libyan Desert (Fig. 7). The minimum angle of $\bar{\theta}_0$ was 39.6° (April 1985), the maximum 50.1° (October 1986), and thus, a median angle of 45° (dashed line) will be used for later normalization purposes.

A compilation of angular albedo models derived from Nimbus 7 scanner measurements used to process the ERBE scanner data was documented by Suttles et al. (1988). Albedos are given for ocean, land, desert, and snow surfaces with clear, partly cloudy, mostly cloudy, and overcast sky conditions for a wide range of solar zenith angles. Approximately three-quarters of the 60° zone is covered by oceans. The remaining quarter has various land types ranging from tropical rain forest to arid deserts. For the present analysis, the ocean portion (75%) was set at 60% partly cloudy and 40% mostly cloudy, and the remaining land portion (25%) was assumed to be partly cloudy land/desert (the 60%/40% cloud settings resulted in a Nimbus 7 model albedo of 0.224 to equal that obtained subsequently for NOAA 9). Area-weighting of the three models provided an estimate of albedo as a function of $\bar{\theta}_0$ for the 60° zone. In the $\bar{\theta}_0 = 40°$ to 50° range, the albedo trend can be linearly approximated as

$$\bar{A}_{\bar{\theta}_0}/\bar{A}_{45°} = 1 + 0.007(\bar{\theta}_0 - 45°). \qquad (9)$$

The $\bar{A}''_{\bar{\theta}_0}$ values for the 7 months were normalized to $\bar{\theta}_0 = 45°$ using Eq. (9) and are plotted in Fig. 14 (diamond symbols). The degradation-corrected solar zenith angle normalized albedo, $\bar{A}''_{45°}$, for $\overline{\text{AJO}}$ 1986 was only 0.4% greater than the 1985 value (Table 6). This small difference is less than the 0.5% interannual variability found in the $\overline{\text{AJO}}$ albedos for the 7-year, Nimbus 7 ERB dataset (Smith et al. 1989). In spite of the many assumptions made during this analysis, it is believed that the sensor degradations are essentially uniform across the response bandwidth, and that the degradation rates determined here for the Libyan Desert are applicable to all scene types.

8. Summary

Sixty-eight months of reflectance measurements from the Libyan Desert (20°–30°N, 20°–30°E) were analyzed in the present paper. The data were obtained during the period from May 1980 to October 1987 from channel 1 (0.57–0.69 μm) of the AVHRR scanners which were on board the NOAA 6, 7, and 9 spacecraft. After being edited for clouds, the data were analyzed with a directional reflectance model which revealed that the NOAA 7 and 9 sensors had incurred substantial degradation during their operation. The degradation rates were determined to be 0, 3.5% and 6.0% per year for the NOAA 6, 7, and 9 spacecraft, respectively. An analysis of the combined data from 30°N to 30°S, which includes half of Earth's surface and many scene types, found that its degradation rates were essentially the same as those for the Libyan Desert suggesting that rates apply to all scene types.

A procedure is given in the paper for determining sensor degradations which basically require only the reflectance measurements and the spacecraft equatorial crossing times. The technique can be applied to future satellite data with only minimal requirements of time and resources.

Acknowledgments. The author wishes to thank Anne C. Wilber for processing the HBP datasets and Stuart R. LeCroy for providing spacecraft ephemeris information. Both are employees of Lockheed Engineering and Sciences Co., Hampton, Virginia.

REFERENCES

Barkstrom, B. R., 1984: The Earth Radiation Budget Experiment (ERBE). *Bull. Amer. Meteor. Soc.*, **65,** 1170–1185.

Darnell, W. L., W. F. Staylor, S. K. Gupta and F. M. Denn, 1988: Estimation of surface insolation using sun-synchronous satellite data. *J. Climate,* **1,** 820–835.

Gruber, A., 1977: Determination of the Earth-atmosphere radiation budget from NOAA satellite data. NOAA Tech. Rep. NESS 76, 28 pp.

——, and J. S. Winston, 1978: Earth-atmosphere radiative heating based on NOAA scanning radiometer measurements. *Bull. Amer. Meteor. Soc.,* **59,** 1570–1573.

——, I. Ruff and C. Earnest, 1983: Determination of the planetary

radiation budget from TIROS N satellites. NOAA Tech. Rep. NESDIS 3, 12 pp.

——, and A. F. Krueger, 1984: The status of the NOAA outgoing longwave radiation data set. *Bull. Amer. Meteor. Soc.*, **65**, 958–962.

Gupta, S. K., 1989: A parameterization for longwave radiation from sun-synchronous satellite data. *J. Climate*, **2**, pp. 305–320.

Schiffer, R. A., and W. B. Rossow, 1983: The International Satellite Cloud Climatology Project (ISCCP)—The first project of the World Climate Research Program. *Bull. Amer. Meteor. Soc.*, **64**, 779–784.

——, and ——, 1985: ISCCP global radiance data set: A new resource for climate research. *Bull. Amer. Meteor. Soc.*, **66**, 1498–1505.

Schwalb, A., 1978: The TIROS-N/NOAA A-G satellite series. NOAA Tech. Memo. NESS 95, 75 pp.

Short, N. M., P. D. Lowman, S. C. Freden and W. A. Finch, 1976: Mission to Earth: Landsat views the world. NASA SP-360, 459 pp.

Smith, G. L., D. Rutan and T. D. Bess, 1989: Atlas of albedo and absorbed radiation derived from Nimbus 7 Earth radiation budget data set—November 1978 to October 1985. NASA RP-1231, 202 pp.

Staylor, W. F., 1985: Reflection and emission models for clouds derived from Nimbus 7 Earth radiation budget scanner measurements. *J. Geophys. Res.*, **90**, 8075–8079.

——, 1986: Site selection and directional models of deserts used for ERBE validation targets. NASA TP-2540, 12 pp.

——, and J. T. Suttles, 1986: Reflection and emission models for deserts derived from Nimbus 7 ERB scanner measurements. *J. Climate Appl. Meteor.*, **25**, 196–202.

Suttles, J. T., R. N. Green, P. Minnis, G. L. Smith, W. F. Staylor, B. A. Wielicki, I. J. Walker, D. F. Young, V. R. Taylor and L. L. Stowe, 1988: Angular radiation models for earth atmosphere system: Volume I—shortwave radiation. NASA RP-1184, 144 pp.

Williamson, L. E., 1977: Calibration technology for meteorological satellites. Atmos. Sci. Lab. Monogr., Ser. 3, U.S. Army, 139 pp.